2022

Spray Deposition of Sustainable Plant Based Graphene in Thermosetting Carbon Fiber Laminates for Mechanical, Thermal, and Electrical Properties

Daniel W. Mulqueen
Old Dominion University

Siavash Sattar
Old Dominion University

Thienan Le
Old Dominion University

Oleksandr G. Kravchenko
Old Dominion University

Original Publication Citation

Mulqueen, D. W., Sattar, S., Le, T., & Kravchenko, O. G. (2022). Spray deposition of sustainable plant based graphene in thermosetting carbon fiber laminates for mechanical, thermal, and electrical properties. *Polymer Composites*, *43*(12), 8696-8714. https://doi.org/10.1002/pc.27051

Received: 30 May 2022 | Revised: 30 August 2022 | Accepted: 1 September 2022

DOI: 10.1002/pc.27051

RESEARCH ARTICLE

Polymer COMPOSITES WILEY

Spray deposition of sustainable plant based graphene in thermosetting carbon fiber laminates for mechanical, thermal, and electrical properties

Daniel W. Mulqueen[1,2] | **Siavash Sattar**[2] | **Thienan Le**[2] | **Oleksandr G. Kravchenko**[2]

[1]Carbon Research and Development Company, Wise, Virginia, USA

[2]Department of Mechanical and Aerospace Engineering, Old Dominion University, Norfolk, Virginia, USA

Correspondence
Daniel W. Mulqueen, Old Dominion University Frank Batten College of Engineering and Technology, Mechanical and Aerospace Engineering, Norfolk, VA, USA.
Email: dan.mulqueen@gmail.com

Oleksandr G. Kravchenko, Department of Mechanical and Aerospace Engineering, Old Dominion University, Norfolk, Virginia, USA.
Email: okravche@odu.edu

Funding information
The Commonwealth Center for Innovation in Autonomous Systems

Abstract

Graphene has generated substantial interest as a filler due to its exceptional strength, flexibility, and conductivity but faces obstacles in supply and implementation. A renewable, plant-based graphene nanoparticle (pGNP) presents a more accessible filler with the same properties as mineral graphenes. In this study, we examine the effects of pGNP, which was sprayed on a carbon fiber/epoxy prepreg at loadings from 1.1 to 4.2 g/m^2. The study considered the mechanical, thermal, and electrical properties of pGNP-composite. An even particle dispersion was achieved using a spray application of pGNP in a water/alcohol suspension with the addition of surfactants and dispersion aides. Results show that pGNP addition increases flexural modulus 15%, flexural strength 17%, interlaminar shear strength 17%, and mode I fracture toughness by 146%, as well as increases electrical conductivity 294% and thermal conductivity 24%, with these improvements observed at 1.1–2.3 g/m^2 spray loadings.

KEYWORDS
curing of polymers, fracture, nanoparticles, thermal properties, electrical properties

1 | INTRODUCTION

Plastic based composite components offer several advantages for OEM parts manufacture, lighter weight, lower cost, and impact resistance, and plastic utilization is growing rapidly, but traditional plastics are constrained by their thermal and electrical conductivity.[1] Thermal conductivity in particular is seeing a growing demand as heat dissipation is of increasing concern for applications for miniaturized electronics to electric vehicle construction.[2] Lack of electrical conductivity still holds back use of reinforced thermosetting plastics in applications where conductivity is essential such as the aerospace industry.[3] Electrostatic painting systems are widely used in automotive coatings but have difficulty with plastic parts because of a lack of electrical conductivity.[4] Plastics are widely used for corrosion resistant tanks and piping, but static build up due to a lack of conductivity creates an explosions hazard.[5] The transition from metal to plastic parts in automotive structures, such as battery enclosures, requires the addition of electrically conductive elements to provide shielding from electromagnetic interference.[6] Carbon nanomaterials, such as graphene, have exceptionally high-carrier mobility which promises dramatic increases in

electrical and thermal conductivity as well as benefits to the physical properties of the plastic parts.[2–5,7]

Graphene nanoparticles (GNP) have shown significant improvements of the thermal conductivity of epoxy composites, at both low and high loadings. When compared to traditional thermal interface fillers, a 5% (v/v) loading of graphene performs as well as 50%–70% (v/v) loadings of alumina or silica.[8] GNP are superior to other carbon nanoparticles in this regard because their large surface area promotes efficient phonon transfer between the matrix and the nanoparticle.[9] A 2021 study with carbon fiber reinforced polyamide 4, 6 have shown increases in thermal and electrical conductivity with GNP addition which have varied between in-plane and through thickness measurements, owing to percolation between the GNP and the carbon fibers. In plane, conductivity was increased 213% and through thickness conductivity was increased 526% at 5% (w/w) loading of graphene, but at these loadings all measured mechanical properties were reduced substantially.[10] Peak increased to thermal conductivity were GNP have increased the decomposition temperatures of thermoplastic materials, but the effect is concentration dependent.[11,12] At loadings up to 2% (w/w), GNP retard the decomposition of the polymer, preventing structural breakdown. Loadings of as little as 0.1% (w/w) have increased the thermal stability of polypropylene by 13°C.[12] At higher loadings, GNP increase the thermal conductivity of the composite, accelerating thermal decomposition.[13] Likewise, graphene has shown a very low percolation threshold for increasing conductivity in polymers.[13] A 0.38% loading of isocyanate treated graphene oxide in polyamide led to a conductivity increase of eight orders of magnitude, along with increasing the strength of the film.[14] An investigation of the anisotropic effects of GNP addition to carbon fiber reinforced plastic (CFRP) composites have shown variance between electrical and thermal conductivity depending on fiber direction. A 6.3% v/v loading of GNP provided a 63% increase in transverse electrical conductivity, while providing an over 300% improvement in the through thickness direction. Through thickness, thermal conductivity was reduced at low GNP loadings before improving by 8% at a 6.3% v/v loading, while transverse thermal conductivity showed moderate decreases in conductivity 0.3% loading.[15] Other, investigations in the through thickness electrical and thermal conductivity of GNP/CRFP composites showed improvements of 132% and 8%, respectively.[16] Experiments using electric fields to orient GNP have shown that thermal and electrical conductivity is impacted by GNP orientation as well, with aligned GNP providing 300% and 27% improvements to through thickness electrical and thermal conductivity as compared to 82% and 20% for unaligned GNP.[17] However, despite promising early results, graphene remains difficult to implement. Even graphene dispersion is essential, as well as good graphene/polymer interaction, however, graphene loading and particle interaction can be too high, increasing agglomeration and reducing conductivity.[18]

Carbon nanomaterials, such as graphene and carbon nanostructures, have a potential in enhancing the interlaminar properties of the composite matrix when used as an interlaminar layer.[19] Interlaminar graphene addition offers multiple benefits over nanoparticle dispersion in resin. First, the uniform dispersion of nanoparticles through the matrix reinforces critical as well as noncritical regions equally resulting in a higher than necessary cost. Secondly, small nanomaterial addition increases the resin viscosity substantially, resulting in difficult processing in resin transfer molding. Spray application of nanoparticles offers a solution to both issues. By not mixing the nanoparticles directly, resin viscosity is not increased and by only applying nanoparticles to critical, interlaminar, areas, costs are optimized.[20] Additionally, in a resin transfer process, the fibers can filter nanoparticles from the resin, creating agglomeration and uneven distribution through the composite.[21] Targeted interlaminar addition of carbon nanoparticles (CNP) have shown increases in fracture toughness[22] as well as functionalization for structural health monitoring[23] and applications in microwave welding.[24] Hand rolling, or coating of graphene interlaminar layers can be time consuming and inconsistent. The use of interleaf layers adds complexity and mass beyond the low mass of interlaminar GNP, as well as potentially interfering with resin impregnation.

Spray application of GNP and other CNP has shown substantial promise in improving fracture toughness in composites. In 2013, the impact of functionalized multiwalled carbon nanotubes (MWCNTs) applied to a prepreg surface were measured with respect to mode I fracture toughness, G_{Ic}. MWCNTs were applied at 0.5% w/w by spray application in an ethanol suspension. Ethanol was chosen over water, acetone, and dichloromethane because of its high-surface energy and low-chemical interaction with the epoxy matrix. A 17% increase in fracture toughness was observed and SEM imaging showed that the improvement derived from the ability of the MWCNT to spread the damage through pullout, peeling and bridging of the particles, as well as from crack displacement from the 10 μm MWCNT rich region to MWCNT poor regions of the matrix. This indicates that the MWCNT are not fully utilized as a reinforcing agent due to crack displacement away from the reinforced regions.[25] A more dramatic improvement was obtained in 2014 using a carbon nanotube (CNT)/methanol spray solution to deposit CNTs at 0.047% w/w onto a 2 × 2

TABLE 1 Energy usage for various means of graphene production

Graphene production method	Energy usage (MJ/kg)	Health and environmental risk
Chemical reduction of graphene-oxide	900–1000[35]	Medium-High[34]
Ultrasonic exfoliation of graphene	70–500[35]	High[35]
Thermal exfoliation	2000[32]	Low[32]
Thermal pGNP conversion	0–545[30]	Low[30]

twill carbon fiber/epoxy prepreg. The resulting composite showed a G_{Ic} improvement of 50%.[26] The highest MWCNT reinforcement was found 2012, where MWCNTs were dispersed into an ethanol solution and sprayed onto woven carbon fiber/epoxy prepregs. The optimal loading was found to be 1.32 g/m^2, at which G_{Ic} was improved by 79% and mode II fracture, G_{IIc}, was improved by 140%. Higher loadings resulted in decreasing mechanical performance. Examination of the composites showed that the MWCNTs moved during curing from the spray surface into the fiber reinforced region, significantly increasing fiber bridging at optimal loading. Investigation of the surfaces with SEM showed that at higher loadings, MWCNTs did not disperse into the matrix, agglomerating on the fracture surface.[21] In 2019, MWCNTs and GNP were compared. Both were applied to unidirectional carbon fiber prepregs with a $[0^\circ]_{30}$ stacking sequence at 1 g/m^2 using an acetone solvent. G_{Ic} values were improved 12.6% for MWCNTs and 101.5% for GNP. SEM analysis showed that GNP perpendicular to the fracture surface exhibit pull-out from the matrix, resulting in a much higher G_{Ic} than neat or MWCNT reinforcement.[27]

While graphene offers several benefits, it has yet to succeed widely in the marketplace for several reasons. Graphene has high levels of Van der Waals self-interaction, which can lead to aggregation and difficulty in dispersion and application.[28,29] Graphene materials have also maintained a high cost, due to short supply of high-quality graphite precursors and difficulty on producing graphene nanoparticles. Another issue which has not been broadly discussed is the carbon emissions and significant environmental impact of graphene production, which was examined in detail in a previous work.[30] Due to increased environmental awareness—as well environmental regulations—composite manufacturers are utilizing new material from renewable, plant based feedstocks.[31] Graphene production from graphite through the chemical reduction of graphene-oxide, ultrasonic exfoliation, and thermal exfoliation are all energy intensive, requiring 70–2000 MJ/kg to produce, utilize several hazardous chemicals and produce hazardous pollutants.[32–35] As shown in Table 1, the energy usage for pGNP production using a combination of natural gas and recovered energy from the thermal decomposition of biomass is substantially lower than thermal exfoliation and chemical reduction as routes for producing GNP. The energy usage is comparable to that of ultrasonic exfoliation of graphene. The energy required to produce pGNP is 545 MJ/kg and fossil carbon emissions are 34.9 kg CO_2/kg pGNP, as shown in Figure 1. Utilization of renewable energy, either from renewable electric generation or from onsite biomass combustion would result in no net CO_2 emissions,[36] giving a range of 0–34.9 kg CO_2/kg pGNP. Further, the CRDC process does not use hydrazine or concentrated acids and does not produce hazardous byproducts. The role of surface functional groups on material properties due to matrix/filler chemical affinity has been shown to be important for GNP composites, with multiple processes being explored to improve the functionality of mineral graphenes and graphene oxides.[12,29,37] The biomass derived pGNP contains a higher number of surface functional groups which increase interaction with simple solvents such as water, alcohol, and acetone resulting in a GNP which can be more easily utilized in simple applications such as spray coating. Further, epoxide functional groups offer opportunities for crosslinking in a thermosetting matrix.

In this study, renewable pGNP are spray-coated between layers of preimpregnated carbon fiber (CF)/epoxy sheets (prepreg). The pGNP/CF/epoxy system is used to examine the mechanical properties (both modulus, strength, and fracture toughness), thermal and electrical conductivity of the complex composite. Increases in thermal and electrical conductivity are desirable, since they increase the range of applications that composite parts may be used in, as well as the range of conditions they will be effective under. This study builds upon previous investigations into the conductivity of GNP enhanced composites by using a plant based pGNP nanoparticle, by examining the suspension and spray properties of the pGNP mixture, and by considering the combined functional and mechanical properties of the composite. The use of pGNP is shown to be distinct from exfoliated mineral GNP in functionality—due to the presence of carboxyl and epoxy functional groups—and morphology. These two factors contribute to improved dispersibility in suspension and provide interlaminar reinforcement of CFRP. A pGNP spray was formulated to provide even pGNP surface application, good surface wetting, and good dispersion. The suspension was designed around spray application, so low-viscosity solvents were chosen. pGNP suspension was improved with dispersion agents. The combined evaluation of functionality and mechanical properties provide

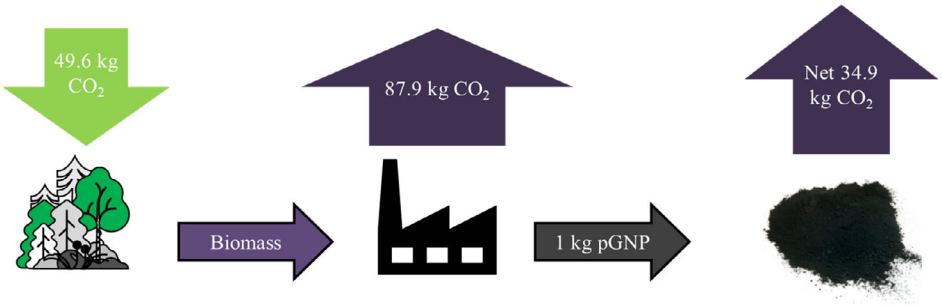

FIGURE 1 Schematic representation of CO_2 flows during pGNP production

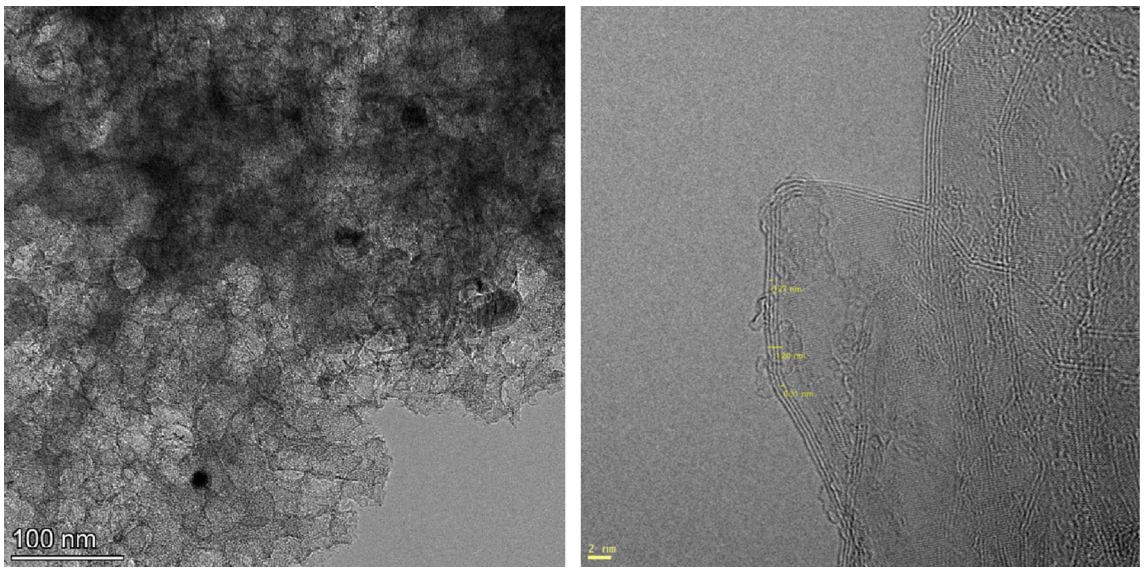

FIGURE 2 TEM scan of plant-based graphene nanoclusters. Interlaminar spacing is 0.345 nm

the trade-off in composite material design to balance thermal and electrical conductivity with strength and fracture toughness. Further, evidence is shown for chemical interaction between the pGNP and the resin and surface micrography is used to present crack deflection as a mechanism for improvements in fracture toughness.

2 | EXPERIMENTAL METHODS

2.1 | Materials

Carbon fiber/epoxy prepreg was purchased from Rock West Composites. The unidirectional prepreg is composed of a Toray T800S fiber (63% w/w) in an intermediate modulus epoxy with a 135°C cure temperature and T_g of 130 ± 10°C. Graphene nanoplatelets were provided by the Carbon Research and Development Company in a 7% w/w suspension with water. Platelet thickness range from 3 to 20 layers (1–6 nm) with a lateral size from 300 to 1000 nm. The nanoplatelets contain both epoxide and carboxyl functional groups, as well as amorphous impurities. TEM imaging, as shown in Figure 2 shows stacked, multilayer graphene crystals with an interlaminar spacing of 0.345 nm. The interlaminar spacing is slightly larger than the 0.335 nm spacing typical of mineral graphene. The multicrystal morphology is more similar to graphene crystals prepared by chemical vapor deposition than exfoliated mineral graphene.

Investigation of surface chemistry via X-ray photoelectron spectroscopy 87.0% C, 10.3% O, 1.4% N, and 1.3% other elements from wood ash. The structure of the carbon bonds on the powder surface, as shown in Figure 3 showed 49.82% sp^2 graphitic/graphene bonding, 36.34% graphene-oxide/epoxide groups (C—O—C) and 13.83% carboxyl groups (O—C═O). Surface C:O ratio is 8.45:1, overall C:O ratio is >15:1, indicating that the majority of oxygen is located in surface functional groups.

2.1.1 | Spray formulation

A GNP spray was formulated using a water/pGNP dispersion along with isopropyl alcohol as well as carboxymethyl cellulose (CMC) and sodium dodecyl sulfate

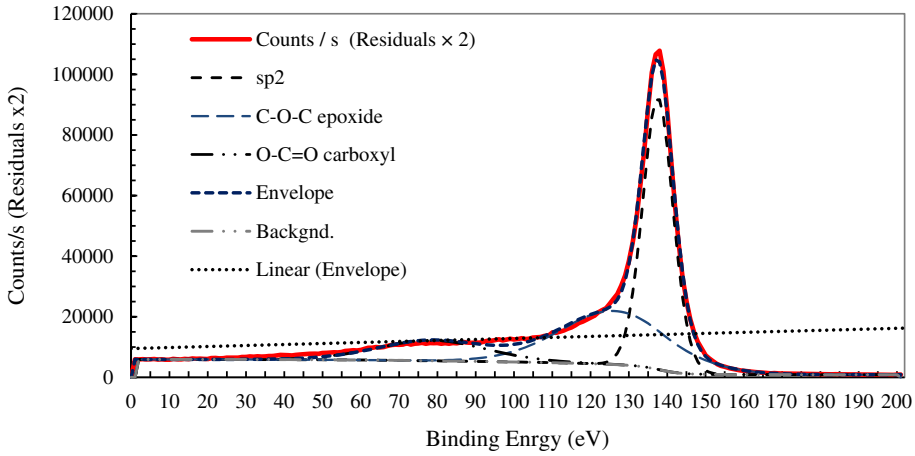

FIGURE 3 XPS analysis of pGNP surface scans

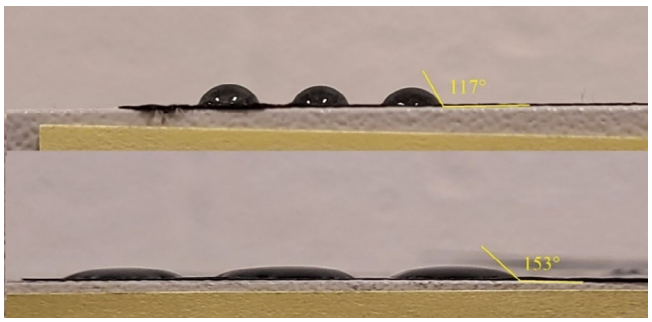

FIGURE 4 Contact angle measurements for pGNP in DI water at 117° and pGNP in 45% IPA with CMC and SDS at 153°

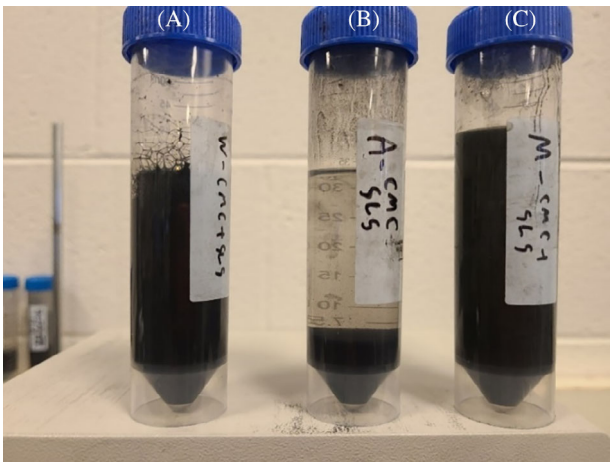

FIGURE 5 pGNP + CMC + SDS dispersions after 48 h resting. (A) In DI water, (B) In 91% IPA, and (C) In 45% IPA. The opaque black color in the left and right samples indicates a much higher pGNP dispersion

(SDS). Water can be a preferred choice over other solvents because of its ease of use and availability, as well as its lack of chemical interaction with the epoxy matrix but water has a much lower surface energy on the epoxy matrix as compared to isopropyl alcohol (IPA) as shown in Figure 4. IPA provides excellent surface wetting on the prepreg surface, as well as being highly volatile to promote fast, even drying but it has poorer dispersion characteristics for the pGNP (Figure 5). Therefore, CMC was used to provide several benefits to the pGNP spray formulation, principally as a binder to promote surface adhesion, while also improving viscosity and surface tension. Addition of CMC also provides benefits to pGNP dispersion. Likewise, SDS is added principally as an anionic surfactant, but it also provides benefits to pGNP dispersion.

To examine the dispersion characteristics and determine a functional spray composition, several mixtures were formulated as shown in Table 2. The supplied pGNP dispersion was diluted with an equal volume of either DI water or 91% IPA. A pGNP/91% IPA dispersion was produced by direct exfoliation of pGNP into IPA. In sets of 50 ml tubes, each pGNP solvent mix was blended with 0.047 g CMC, 0.220 g of SDS, both 0.047 g CMC and 0.220 g of SDS, or neither. All samples were blended on a high shear mixer for 10 min to thoroughly mix all components. The contact angle, CA, was measured shortly after mixing on a sheet of uncured prepreg using the sessile drop method. The mass of dispersed solids was measured after 48 h of settling time by drying a volume of the suspension and measuring the remaining solid matter. As shown in Table 2, the 91% pGNP/IPA dispersion exhibited the best surface wetting, with a 180° contact angle, but very poor dispersion of pGNP and was deemed unsuitable for further exploration. An addition of CMC and SDS to pGNP in water provided the best dispersion at 5.60 g/L but relatively poor surface wetting at a contact angle of 123.4°. pGNP with CMC and SDS in 45% IPA provided the best balance of dispersion at 4.68 g/L with relatively good surface wetting with a contact angle of 152.9°. pGNP spray solution was prepared by combining 210.56 g of graphene/water slurry with 1.8513 g of SDS, 0.3846 g of CMC, and 171.3 g of 91% IPA and mixing until the SDS and CMC were thoroughly dissolved.

TABLE 2 Dispersibility, in g/l, and contact angles (CA) of pGNP in water and 45% IPA with CMC and SDS additives

	DI water		91% IPA		45% IPA	
	g/l	CA	g/l	CA	g/l	CA
pGNP	0.40	117.3°	0.13	180.0°	0.40	144.8°
+CMC	3.31	119.0°	0.09	156.1°	5.05	156.2°
+SDS	2.50	116.4°	0.53	158.4°	5.61	152.9°
+CMC + SDS	5.60	123.8°	0.48	162.3°	4.68	152.9°

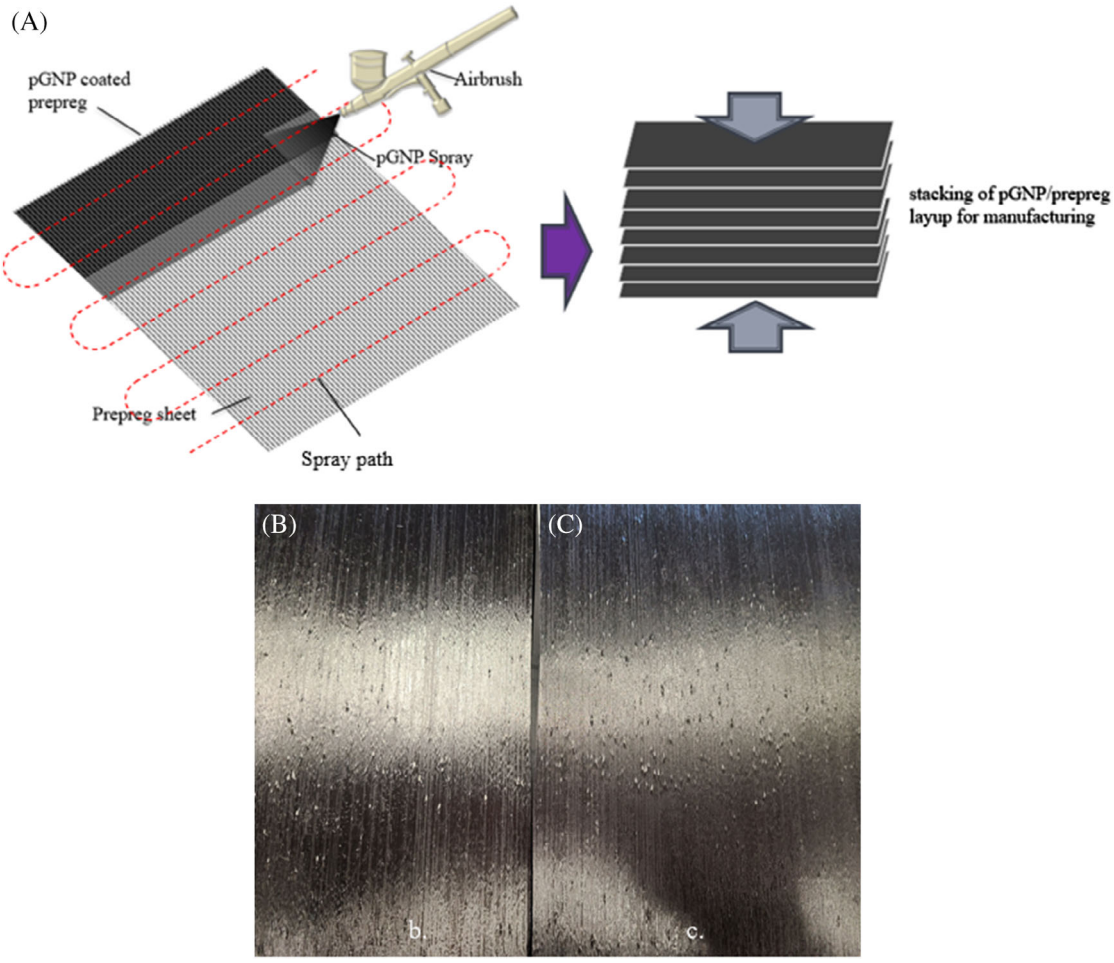

FIGURE 6 (A) pGNP spray application. (B) CF prepreg before spraying. (C) CF prepreg with nGNP coating

2.1.2 | Composite fabrication with pGNP in interlaminar region by spray deposition

CF/epoxy prepreg sheets were treated with pGNP by spraying the prepared suspension through an airbrush onto the sheets by hand while controlling that distance between the airbrush and the prepreg sheet was about 0.2 m. To coat CF/epoxy prepreg sheets with pGNP, an initial weight was taken before the sheets were hung vertically. The pGNP spray suspension was applied using a Central Pneumatic 93,506 airbrush using even, overlapping passes as shown in Figure 6A. Light coatings were used in order to ensure uniformity and to prevent beading on the prepreg surface. Coatings higher than 1.1 g/m^2 were sprayed in multiple coats. Application rates were estimated by volumetric flow rate during application, precise pGNP loading was measured by weighing the sprayed sheets after sufficient drying. The coated surface (Figure 6C) is slightly less reflective than the uncoated surface (Figure 6B).

Coating uniformity was estimated using electrical resistance with a Cen-Tech p37772 digital multimeter, taking an average of five points on dried surfaces, at least

10 min after spraying. Electrical conductivity across the surface of the dry, uncured ply was measured using an ohmmeter with a resistance of 17 Ω/mm, spray with the GNP solution at 1.1 g/m^2 reduced this to 1.8–3 Ω/mm. Further exploration of this is warranted.

Samples for curing temperature, electrical, and thermal conductivity were produced by stacking total of 168 5 cm × 5 cm plies with [0°] orientation to a total thickness of 2.5 cm. Larger prepreg sheets were sprayed before cutting into 5 cm × 5 cm plies and these plies were stacked with the pGNP sprayed surfaces laid against the untreated, paper backed surfaces with backing removed, providing interlaminar pGNP layers between each ply. A thermocouple was placed between plies 84 and 85, in the center of the sample to measure the heat reached internally.

2.2 | Material characterization of fabricated pGNP composites

2.2.1 | Microscopy

Scanning electron microscopy (SEM) was performed using a Zeiss Supra Microscope with 30 μm aperture and 5 kV accelerating voltage with a minimum of 200 individual particles measured to provide a statistically significant distribution of particle lateral size. The image analysis was carried out using SPIP™ (Version 6.7.9). The lateral size of each particle was determined by measuring the length (longest edge-to-edge distance) and width (a perpendicular bisector of the length) of the particles and calculating the mean value of the two. Transmission electron microscopy (TEM) was performed using an FEI Talos F200X with 0.16 nm resolution and 200 keV accelerating voltage.

X-ray photoelectron spectroscopy (XPS) was carried out in ultra-high vacuum using a Kratos Axis Ultra DLD instrument. A monochromated aluminum X-ray source was operated at 75 W (15 kV, 5 mA) emission. Each analysis area was approximately 700 μm × 300 μm, and the depth of information in XPS is less than 10 nm.

2.2.2 | Viscosity measurements

The viscosity of the pGNP suspensions was measured using an Anton Paar MCR 302 Rheometer with a T-PTD 200 tribology cell and a 25 mm, parallel plate testing head with a 1 mm test height at 25°C. Viscosity was measured across a range of shear rates, from 1 to 1000 s^{-1} to examine both the impact of SDS and CMC added to pGNP suspensions, and potential non-Newtonian behaviors of the suspension. Shear thinning is preferable for spray formulations where low viscosity at high shear rates improves spraying performance while low viscosity at lower shear rates prevents sagging of the sprayed surface and improves long-term suspension stability.[38,39]

2.2.3 | Temperature evolution inside of the thick composite

To observe the effects of thermal conductivity and changes to curing kinetics on the curing of large composite members, composite samples were produced by stacking 168 plies with planar dimensions of 5 cm × 5 cm to a total thickness of 2.5 cm. The high thickness of the sample was used to provide a better representation of the cure exotherm. A thermocouple was placed in the center of the sample at the location of the midplane of the layup, shown in Figure 7A,B. This allows monitoring of the temperature evolution in the middle of the laminate, where the highest temperature peak is expected to occur due to the heat transfer and cure exotherm. These samples were cured under vacuum on a flat mold in a convection oven, without additional pressure and were heated at a rate of 2.8°C/min to 135°C for 120 min, while internal temperatures were logged.

2.2.4 | Differential scanning calorimetry

Differential scanning calorimetry (DSC) is a thermal analysis method for obtaining the cure kinetics and degree of cure of a thermoset composite material and was used to measure the impact of interlaminar pGNP on cure kinetics. For this test, two ply composite samples were produced from 13 cm × 13 cm sheets of the prepreg, one pair was left untreated, and another pair of sheets were sprayed with pGNP at approximately 2 g/m^2 and allowed to dry. Untreated sheets of prepreg were pressed into a two ply composite. The sprayed faces of pGNP treated plies were pressed together, giving a 4 g/m^2 interlaminar density. A 2.5 mm × 2.5 mm specimen was cut from the center of each laminate and analyzed in a Shimadzu DSC-60A apparatus using aluminum pans under nitrogen atmosphere with dynamic and isothermal heating against reference samples. For dynamic testing, the specimens were heated to 300°C with a rate of 10°C/min. For isothermal testing, the specimens were heated to 135°C and held for 120 min. Heat flow through the sample was measured by the instrument under heating and logged and the cure of the composite is shown by a characteristic curve which shows the region where the cure is exothermic.

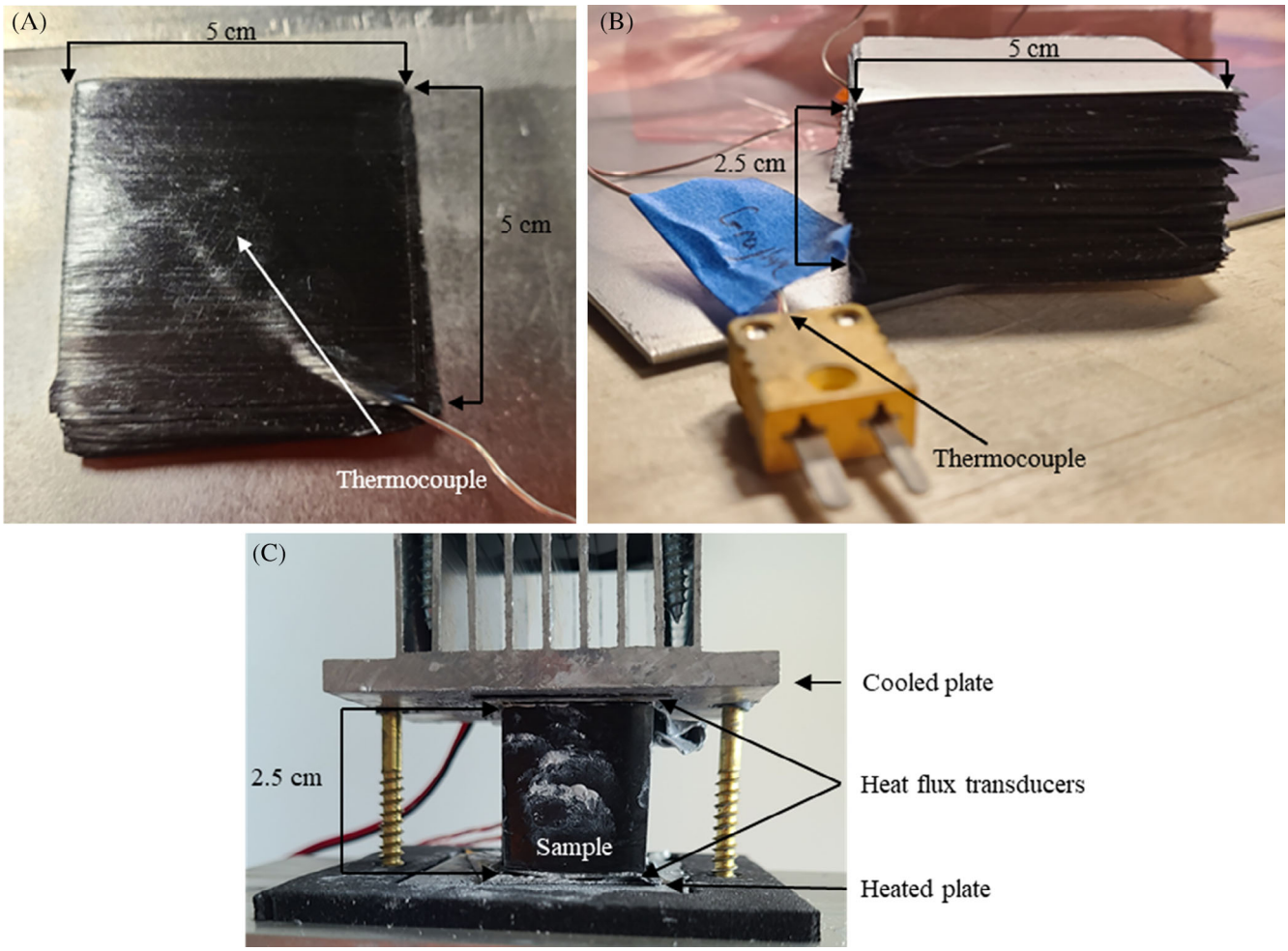

FIGURE 7 (A) A thermocouple (junction indicated by the white arrow, leads visible in the lower right) placed in the uncured composite, between plies 83 and 84. (B) A 168 ply, 2.5 cm thick composite with thermocouple inserted before curing. (C) A profile of the thermal conductivity test apparatus

The degree of cure, α, at time, t, is measured by comparing the heat of cure at temperature, ΔH_i, as defined by the integral of the rate of heat generation, dQ/dt, from 0 to t as given by,

$$\Delta H_i = \int_0^t \left(\frac{dQ}{dt}\right) dt \quad (1)$$

To the total heat of cure, ΔH_T to the total heat of reaction as given by the integral of dQ/dt from 0 to t_t, the time required to complete the cure, as shown in the following equation:

$$\Delta H_t = \int_0^{t_t} \left(\frac{dQ}{dt}\right) dt \quad (2)$$

Such that:

$$\alpha = \Delta H_i / \Delta H_t \quad (3)$$

2.2.5 | Thermal conductivity

After curing, the composite samples from the curing temperature tests were cut into four smaller pieces, approximately 2.5 cm × 2.5 cm × 2.5 cm. Thermal conductivity was measured by placing the composite samples in between two Omega HFS-5 heat flux sensors sandwiched between plates of a heat flux apparatus as shown in Figure 7C. The heated plate of the apparatus was heated with a thermoelectric heater under a constant 9 V DC, the cooled face was actively cooled with 20°C air. Heat flux sensors were wired to an Omega HFS-DAQ data logger and values were recorded to a log file. Thermally conductive paste, Omega OT-201-2, was used between all contact faces. The measured heat flux was averaged between the two sensors and used to calculate thermal conductivity. A 304 stainless steel control sample measuring 2.5 cm on all sides was used for calibration. Measurements in each sample were taken in three dimensions relative to the fiber direction: longitudinally, along the

fiber length (direction 1); in-plane, transverse to the fibers (direction 2); out-of-plane, through the thickness of the composite (direction 3). Thermal conductivity for the sample was calculated according to the heat flux equation,

$$k = xQ/\Delta T \tag{4}$$

where k is the thermal conductivity of the sample in watts per meter-Kelvin (W/[m °K]), ΔT is the temperature differential across the sample in Kelvin (°K), x is the thickness in meters (m), and Q is the average heat flux across the sample in watts per square meter (W/m^2).

2.2.6 | Electrical conductivity

Electrical measurements were performed on the same samples as were used in thermal conductivity tests. Electrical resistance was measured using a Cen-Tech p37772 digital multimeter across the sample in the fiber direction (1), perpendicular to the fiber direction (2), and in the out-of-plane direction across the composite thickness (3). Resistance was converted to conductivity in milli-Siemens per centimeter (mS/cm) following the equation,

$$\kappa = \rho/x \tag{5}$$

where κ is the conductivity in siemens per meter (S/m), ρ is the measured resistance in ohms (Ω), and x is the thickness of the sample in meters (m).

2.2.7 | Flexural and short beam testing

Composite beam samples were prepared within the guidelines of ASTM D790 and D2344 using 26 plies of prepreg with a [0°] stacking sequence, with interlaminar pGNP addition between each ply. Composite beams were cut from larger prepared plates. Five beams were tested for each condition.

Flexural modulus and strength were measured on a Ektron TS2000 universal testing apparatus in a three-point bending fixture in accordance with ASTM D790. Beams, approximately 4 mm thick and 13 mm wide, were measured across a 70 mm span. The flexural modulus, E, is calculated by measuring the slope of the stress over strain in the linear region of deformation.

$$E = 3P_c/4bh \tag{6}$$

where P_c is the critical load b is the beam width, and h is the beam thickness. Flexural strength, σ_f, is calculated using Equation (7):

$$\sigma_f = 3P_c l/2bh^2 \tag{7}$$

where l is the span length.

Interlaminar shear strength (ILSS) was evaluated with short beam testing following ASTM 2344 using a 35 mm span. ILSS, given by F_{31}, is calculated by Equation (8):

$$F_{31} = 3P_c/4bh \tag{8}$$

2.2.8 | Mode I fracture

For mode I fracture, large composite panels were prepared within the guidelines of ASTM D5528 by stacking 26 plies of prepreg with a [0°] stacking sequence, resulting in a final panel approximately 4 mm thick. To create an initial crack, a 30 μm Teflon film was included between the 13th and 14th plies, perpendicular to the fiber direction, across the top 50 mm of the sheet. For the graphene impregnated composite, a single GNP interlaminar layer was applied between plies 13–14. Test beams were cut from the cured panels on a bandsaw to the test dimensions at a width of 20–25 mm. The edges of beams were painted with a white correctional fluid to improve crack visibility, and markings were added to track crack growth to the nearest millimeter. Steel hinges were glued to the ends of sample beams using a cyanoacrylate gel adhesive. Five beams were tested for each condition.

Double cantilever beam (DCB) tests for mode I fracture were performed following the ASTM D5528 standard on an Ektron TS2000 universal testing apparatus as shown in Figure 8A. Mode I fracture toughness, G_I, was calculated using the Compliance Calibration (CC) method following ASTM D5523-13. The test beam was loaded from the hinges until the crack front propagated 5 mm, before unloading and repeating the loading/crack extension for eight cycles. A plot of log (δ_i/P_i) over log(a_i) was generated from test data at each measured crack length and a line of best fit was generated with a slope of n, ranging from 2.5 to 3.3 for the sampled beams. The compliance factor n is used to calculate the interlaminar fracture toughness as follows:

$$G_I = nP\delta/2ba \tag{9}$$

where P is the load, δ is the load point displacement, b is the sample width, and a is the crack length at fracture.

2.2.9 | Mode II fracture

Mode II fracture was tested according to ASTM D7905 on the fractured mode I test specimens. Five beams were

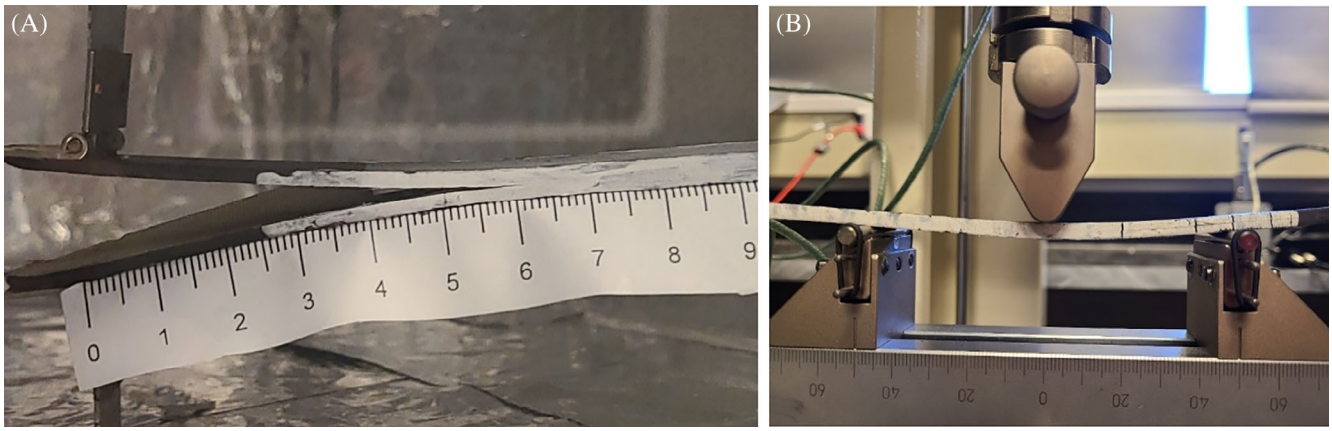

FIGURE 8 (A) Mode I DCB testing configuration; (B) mode II ENF testing configuration

tested for each condition. Mode II interlaminar fracture toughness, G_{IIc}, was measured on a three-point bending fixture following ASTM D7905 ad shown in Figure 8B. Test beams were set such that the crack tip was a fixed distance from one of the support rollers ($a_0 = 20$ mm and $a_0 = 40$ mm) and loaded at 0.5 mm/min to approximately 50% of the estimated critical force (P_c). The test, at $a_0 = 30$ mm, is destructive and is loaded until the crack extends at P_c. A compliance coefficient, m, is calculated according to the formula:

$$\delta_i/P_i = A + ma^3 \tag{10}$$

Mode II interlaminar fracture toughness, G_{IIc}, is given by the equation:

$$G_{IIc} = 3mP_c^2a_0^2/2b \tag{11}$$

where m is calculated from Equation (7), P_c is the critical load, a_o is the initial crack length (30 mm) and b is the beam width. The compliance value, m, varied depending on pGNP loading and temperature. Untreated beams had m values of 0.023–0.040 with 2.3 g/m^2 pGNP m values of 0.018–0.019.

3 | RESULTS AND DISCUSSION

3.1 | Viscosity measurements

The viscosity measurements of the pGNP suspensions are detailed in Table 3, below. The 45% IPA, pGNP mixture shows a higher viscosity than water. CMC addition increases the mixture slightly in all cases, while SDS addition increases viscosity dramatically in water but trivially in IPA solutions.

TABLE 3 Viscosity of pGNP suspensions in water and 45% IPA with CMC and SDS additives

	DI water, η [mPa s]	45% IPA, η [mPa s]
pGNP	2.089 ± 0.991	4.223 ± 0.943
+CMC	2.206 ± 0.0.166	5.263 ± 0.983
+SDS	17.093 ± 34.250	4.148 ± 1.135
+CMC + SDS	1.918 ± 0.204	6.155 ± 3.278

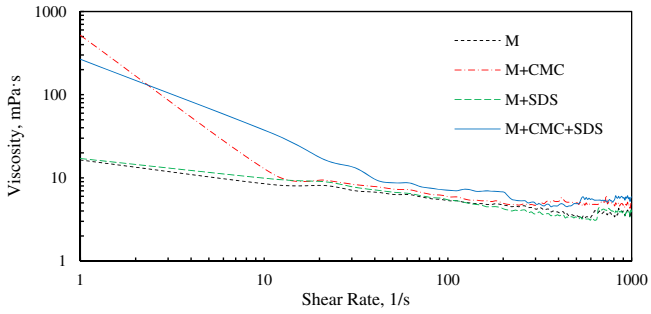

FIGURE 9 The viscosity of 45% IPA suspensions measured at shear rates of 1–1000 s^{-1} show moderate shear thinning for the neat and SDS mixture, but more dramatic shear thinning for the CMC and CMC + SDS suspensions

The viscosity profiles for the 45% IPA suspensions are shown in Figure 9. All suspensions show shear thinning with increasing shear rates, with the CMC containing suspensions showing this to a much greater extent. In the 45% IPA, the CMC and CMC + SDS suspensions increase viscosity at 1 s^{-1} to 516 and 267 mPa s, respectively, from 17 mPa s in the suspension with no additives. These viscosity profiles are well suited to a spray mixture. Low viscosity at high shear rates improves spray performance of the suspension because it requires less energy and produces a finer spray, where a high viscosity at low shear rates prevents

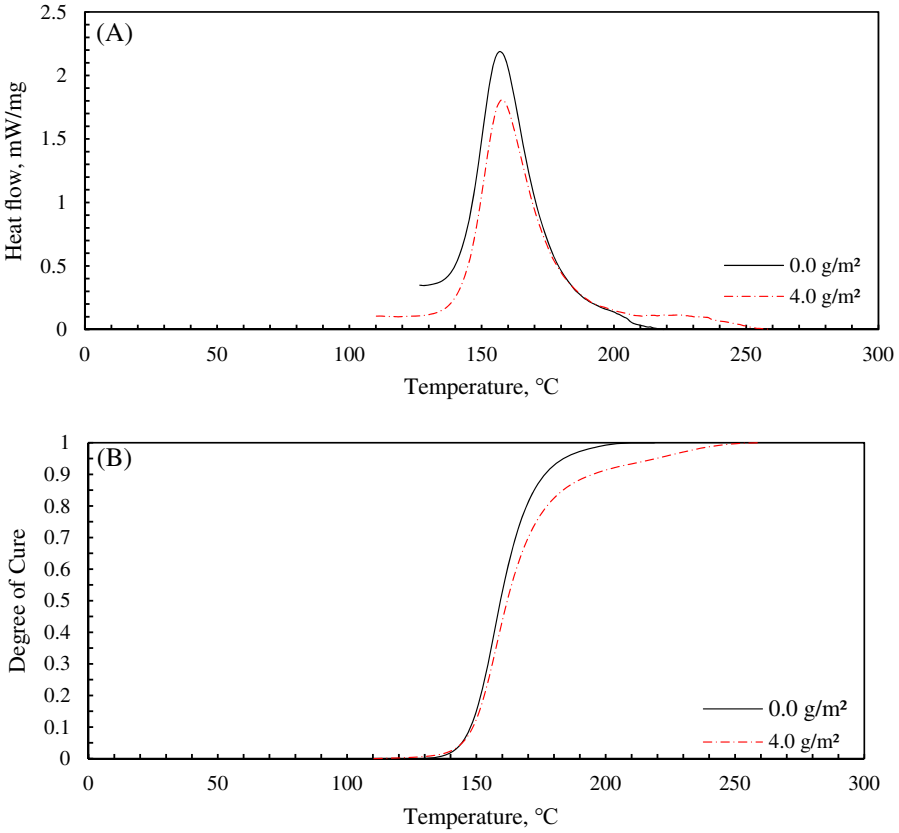

FIGURE 10 (A) Exotherm profiles of curing pGNP/CRFP and neat CRFP under dynamic heating, (B) the degree of cure with heating of pGNP/CRFP as compared to neat CRFP

dripping and sagging during drying and reduces the settling of particles over time.[38,39] The addition of CMC to the suspension provided the greatest improvement to low shear viscosity, without negatively impacting viscosity at high shear rates. The lack of viscosity improvements with SDS in alcohol is not surprising, since SDS is a salt and IPA is much less polar than water.[40] As a surfactant, SDS reduced the surface tension of the liquid in the suspension, and the tension at the graphene/liquid interface which improved nanoparticle wetting and particle suspension.[41]

Wetting on the prepreg surface is important for even distribution of the spray, while particle suspension is important for uniform suspension concentration and stability before spray is applied. This effect is present in each solvent but is most striking in the 45% water/IPA mixture where suspended solids are increased from 0.40 g/L for water/alcohol alone to 5.61 g/L with SDS addition. The increase in low shear rate viscosity with CMC addition is expected and provides the combined benefits of improving spray performance (as discussed earlier), nanoparticle suspension, and improvements in surface wetting. The high viscosity at low shear rates helps to keep nanoparticles from settling which is a key element in dispersing particles. The CMC addition was most effective in the 45% water/IPA mixture as well, with an increase in suspended solids from 0.40 to 5.05 g/L. CMC addition increased viscosity at 1 s^{-1} shear rate from 17.1 to 516.4 mPa s. The combined particle dispersion with CMC and SLS was reduced slightly in the water/alcohol mixture from CMC or SDS alone, but the overall combination of properties of the suspension was optimized using CMC and SDS in the 45% water/IPA mixture.

3.2 | Differential scanning calorimetry

DSC exotherms of the treated and untreated composites in dynamic heating are shown in Figure 10A. The peak heat flow is slightly lower in the pGNP sprayed composite, 1.70 versus 1.84 mW/mg, but the time of reaction is extended for the pGNP sprayed composite. The total heat to cure is almost identical in both cases: 114 J/g for the pGNP/CRFP versus 112 J/g for the neat CRFP. The exotherm for pGNP treated composite has a distinctive shoulder at higher temperatures, indicating changes to the cure kinetics due to the presence of pGNP. The degree of cure for the treated and untreated composites are shown in Figure 10B. The degree of cure in pGNP/CFRP initiates at lower temperature, 110°C versus 126°C in neat CFRP, and completes at a higher temperature, 259°C versus 218°C in neat CRFP.

Isothermal DSC exotherms are shown in Figure 11A and degree of cure is shown in Figure 11B. As with the dynamic heating, the peak heat flow is lower in the pGNP treated composite, 0.60 versus 0.71 mW/mg for neat CRFP. The time of reaction is extended for the pGNP sprayed composite, 78 min versus 64 for neat CRFP. Similar to dynamic test, the total heat to cure is unaffected by pGNP: it is 117 J/g for the pGNP/CRFP versus 120 J/g for the neat CRFP.

3.3 | Thermal conductivity

The impact of pGNP addition was unique for each material direction with respect to the fiber orientation as shown in Figure 12. In the fiber direction thermal conductivity decreased at 1.1 g/m^2 before increasing at higher loadings to a total of 7.13 W/(m K), an 18% improvement. In the transverse direction 1.1 g/m^2 showed an increase of 24% but higher loadings reduced thermal conductivity. Through thickness thermal conductivity was decreased with pGNP addition at all levels to a maximum of 40%. Similar fluctuations have been shown in previous studies, with decreases in conductivity at lower loadings and increases at higher loadings,[15] although the magnitude of variation shown is greater than has been previously observed. Orientation of pGNP due to spray application may play a role in the observed anisotropy.[17] The loss in thermal conductivity in the transverse and cross plane directions can be attributed to the increase in void volume in the composite at higher pGNP loading.

3.4 | Temperature evolution in a thick composite in the presence of pGNP

The recorded temperature evolution is a product of both through thickness conductivity and heat of reaction. DSC testing shows a lower peak heat of reaction with pGNP which would indicate a lower peak temperature during curing while K_{33} was lowered with pGNP addition, indicating a higher peak temperature. The temperature evolution was measured to evaluate how the peak temperature in a thick section will change with interlaminar pGNP. The temperature profiles of pGNP treated composites show an increase to the maximum temperature reached during curing with increasing pGNP loading, as shown in Figure 13A. Peak temperatures are given in Table 4. A negligible difference in internal curing temperature was observed at 1.1 g/m^2 loading, after which the internal temperature rose substantially with increased loadings to a total of 9.3°C at 4.2 g/m^2. This corresponds with the specific gravity of the cured composites, shown in Table 5. There was no increase in void

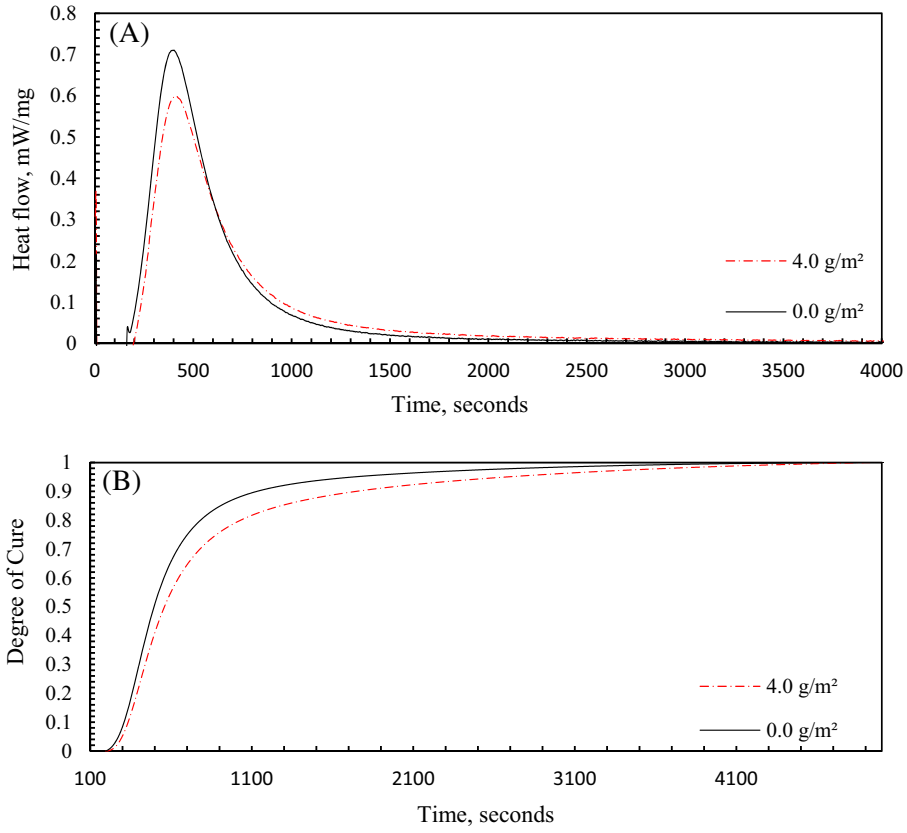

FIGURE 11 (A) Exotherm profiles of curing pGNP/CRFP and neat CRFP under isothermal heating at 135°C, (B) the degree of cure over time of pGNP/CRFP as compared to neat CRFP

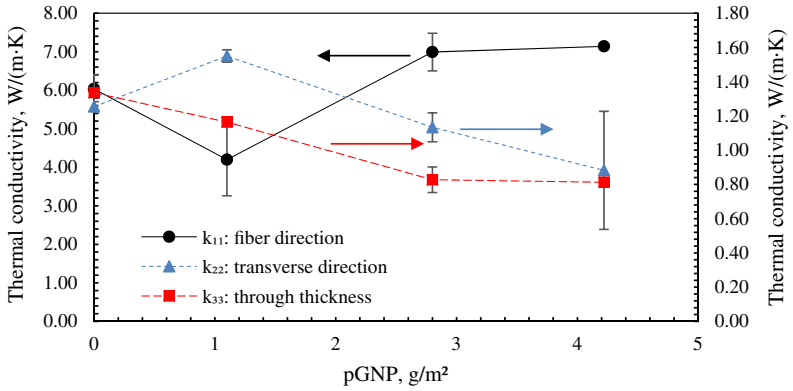

FIGURE 12 The thermal conductivity of composites at various pGNP loadings in three principal directions

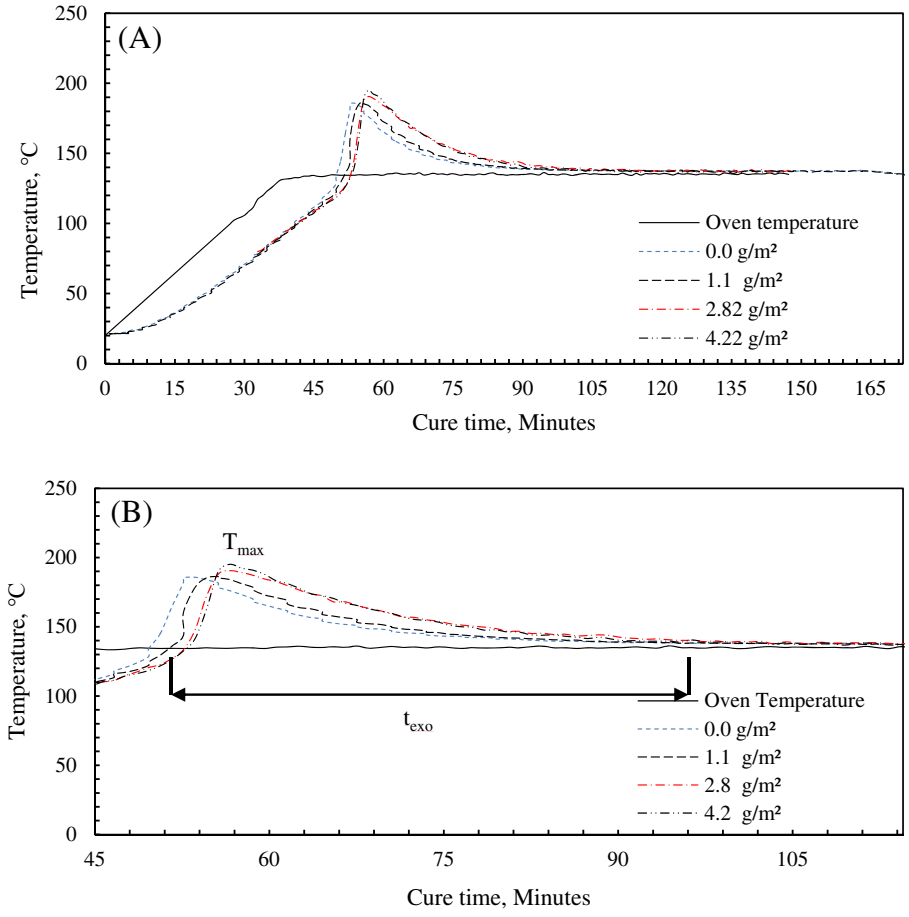

FIGURE 13 (A) Exotherm profiles of curing composite blocks at various graphene loadings, with the oven air temp as a reference. (B) details of the exotherm duration and peak temperature are shown

volume at 1.1 g/m^2 loading, but 4.2 g/m^2 loadings produced a void volume of 0.08. Similar void formation has been shown in other work.[16] This void formation is connected to reductions in thermal and electrical conductivity, as well as flexural modulus, which has not been investigated as a mechanism in studies with similar results.[15] There is also a slight delaying of the exothermic cycle with increased loading and a decreased exotherm with increasing pGNP content, visible from the time versus temperature profile. As the loading increased, the duration of the period in which core temperature exceeded oven temperature increased from 40 min for the neat sample to 41 min for 1.1 g/m^2, 46 min for 2.8 g/m^2, and 47 min for 4.2 g/m^2 loadings, as shown in Figure 13B. This corresponds with isothermal DSC results (shown in Figure 11) which show a similar delaying and elongation of the exothermic cycle with interlaminar pGNP. The lower heat flow peak in pGNP composites from DSC is opposite to the higher temperature peak which was observed during the thick laminate cure. These results show the combined impact on curing temperature from change to curing kinetics and void formation, both of which result from chemical interaction between the pGNP and the resin system.

TABLE 4 Maximum curing temperature of pGNP treated composites

Loading	Coating density, g/m^2	Resin mass fraction, %	Maximum temperature, T_{max} (°C)	Duration of exotherm peak, t_{exo} (min)
0.0 g/m^2	0	0.0%	185.84	40
1.1 g/m^2	1.1	1.3%	186.35	41
				153
2.8 g/m^2	2.8	3.3%	191.36	46
4.4 g/m^2	4.2	4.9%	195.16	47

TABLE 5 Specific gravity and void fraction of composites

Loading	g/ml	Void fraction
0.0 g/m^2	1.443 ± 0.051	0.000
1.1 g/m^2	1.470 ± 0.017	0.000
2.8 g/m^2	1.340 ± 0.017	0.077
4.4 g/m^2	1.337 ± 0.040	0.080

3.5 | Electrical conductivity

Electrical conductivity was increased with increased pGNP loading but the increase varied depending on the axis of measurement. As shown in Figure 14, in the transverse and cross plane directions (2- and 3-principal material directions) there is a diminishing return in conductivity after 1.1 g/m^2, with plateauing values at 2.8 and 4.2 g/m^2, showing that the percolation threshold has been reached. The impact of void formation is clear at 2.8 g/m^2 loading, where reductions in conductivity in all directions is apparent. Ultimate increases at 4.2 g/m^2 of 199% and 119% in the transverse and cross plane directions, respectively, are only marginally higher than the improvements at 1.1 g/m^2 of 188% and 94%. These values are negatively impacted by void content. Conductivity improvements in the fiber direction show their greatest marginal gain at 1.1 g/m^2 loading at 156% but continue to increase to 294% at 4.2 g/m^2. While anisotropy in improvements with GNP addition have been shown, these results differ from past results which showed greater relative improvements in through thickness conductivity over transverse conductivity.[15] In the fiber direction, interactions between the conductive fibers and GNP have been shown to improve conductivity and lower the percolation threshold,[16] however the percolation threshold in this study has not been reached at 4.2 g/m^2, despite being reached in the transverse and through thickness directions. Other studies have shown greater improvements in through thickness conductivity (132%–300%) as compared to transverse conductivity (63%) in VARTM processes, due to the higher relative impact of graphene in the resin rich, interlaminar regions, while transverse conductivity has been dominated by fiber contact.[15,16] The relative increase in this work is consistent with the thermal conductivity findings that pGNP orientation as a result of the spray application process appears to play a significant role in anisotropic properties.

3.6 | Flexural and short beam testing

The flexural modulus and strength of the pGNP treated composites were increased at 1.1 g/m^2 loadings, as shown in Figure 15A, by 15% and 17%, respectively. Representative results of the three-point bending test are shown in Figure 16A. At higher loadings the modulus decreases below the untreated value by 16% and the strength plateaus with a 12% increase. The peak values at 1.1 g/m^2 correspond to the increase in void volume with higher loadings, as the void fraction begins to offset or overcome improvements from the pGNP addition. Short beam test results are presented in Figure 15B, with representative results shown in figure 16B. A 2.8 g/m^2 loading of pGNP improved ILSS, F_{31}, of composites by 17% over neat samples while a 4.2 g/m^2 loading only resulted in a 6% increase.

Increases to ILSS are expected as the interlaminar strength is a property of the load transfer between plies where pGNP is able to contribute to both the interlaminar reinforcement—which dominates the interlaminar load transfer—and provide crack deflection mechanism, as discussed later in fracture toughness results. The improvements to flexural strength can be interpreted as an extension of improvements to ILSS, which allow load to be transferred more effectively between the plies. This mirrors similar results with GNP in glass fiber composites.[42] Flexural modulus improves 15% at 1.1 g/m^2 before the void formation at higher loadings reduces the matrix stiffness. As a result, 1.1 g/m^2 pGNP loading created an interlaminar region which was both stiffer and stronger than the untreated epoxy, but higher loadings produce a composite which is less stiff, due to the presence of the voids, but maintains a higher ultimate strength as compared to the untreated composite.

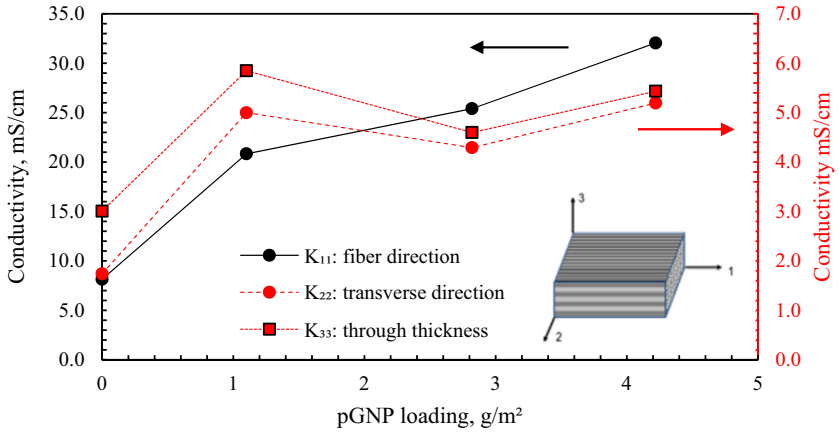

FIGURE 14 The electrical conductivity of composites at various pGNP loadings in three principal directions

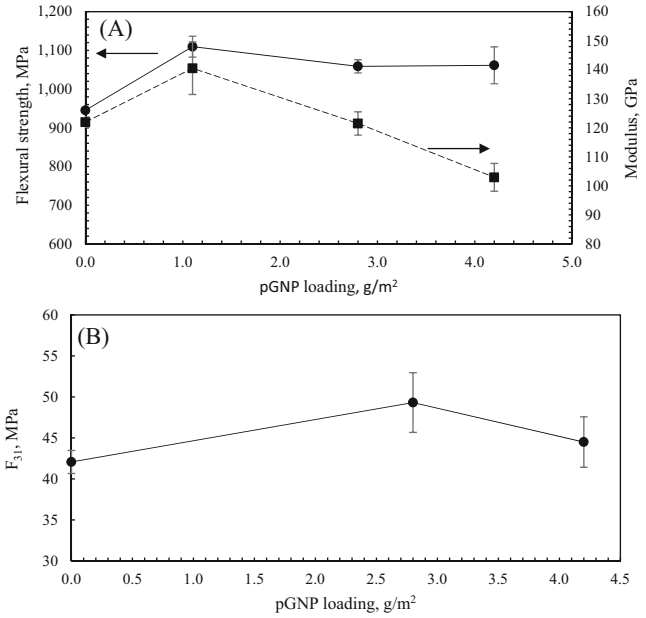

FIGURE 15 (A) Flexural strength and modulus of pGNP treated composite beams. (B) F_{31} values for CF/epoxy beams at 0.0, 2.8, and 4.2 g/m^2 pGNP loadings

3.7 | Fracture toughness testing

Figure 17 presents representative load–displacement curves for composite samples. Mode I fracture was tested at a loading of 2.3 g/m^2, a value chosen to maximize improvements without significant void formation. Results for the DCB testing of neat and pGNP treated composites are presented in Figure 18. The pGNP treated samples were 146% tougher than the neat samples at initial crack extension. This is a marked improvement over previously published increases of 79% for MWCNT[21] and 101.5% for sprayed GNP.[27] This result corresponds with the results for flexural and short beam testing, which show that interlaminar pGNP addition through spray application provide substantial increase to the strength of the epoxy matrix and the matrix/fiber interface in the interlaminar region. Bonding between pGNP functional groups and the epoxy matrix plays a key role in improving the fracture toughness. Over the first 25 mm of crack extension pGNP treated composites were 53% tougher than neat composites. Micrographs of the fracture surface, as shown in Figure 19, highlight the increase in fracture surface roughness of the pGNP treated sample. The zero point in surface roughness measurements was obtained from focusing on the flat region of the Teflon insert, prior to crack extension. The increase in roughness represents an elongation of the crack front, which increases the energy required to extend the crack front. The untreated composites exhibited more variability in G_{Ic} than the pGNP treated composites at greater crack extension. Typically, increases to G_{Ic} with crack extension represent fiber bridging, an artifact of DCB testing, which depend on the fiber migration into the interlaminar region between the neighboring plies.[43] A reduction in fiber bridging may represent improvements to fiber/matrix interactions with nanoparticle additions which have been observed in other studies.[21,44,45] The presence of pGNP in the interlaminar region instead appears to inhibit this process, therefore, the full increase in G_{Ic} of pGNP-composite can be attributed to crack deflection, as discussed previously. As the crack extension increased, fiber bridging became a substantial factor in all cases resulting in reaching a plateau behavior in G_{Ic} propagation values, with the greatest relative impact observed in the untreated composite.

Results for the end notch flexural testing of neat and pGNP treated CF/epoxy composites are presented in Figure 20. The mode II interlaminar fracture toughness, G_{IIc}, of composites with and without pGNP interlaminar spray did not change. Previously published improvements to G_{IIc} with CNP addition show a mix of high reinforcement from 40%[46] to 140%[21] as well as low reinforcement of 7%.[47] SEM analysis of the fractured

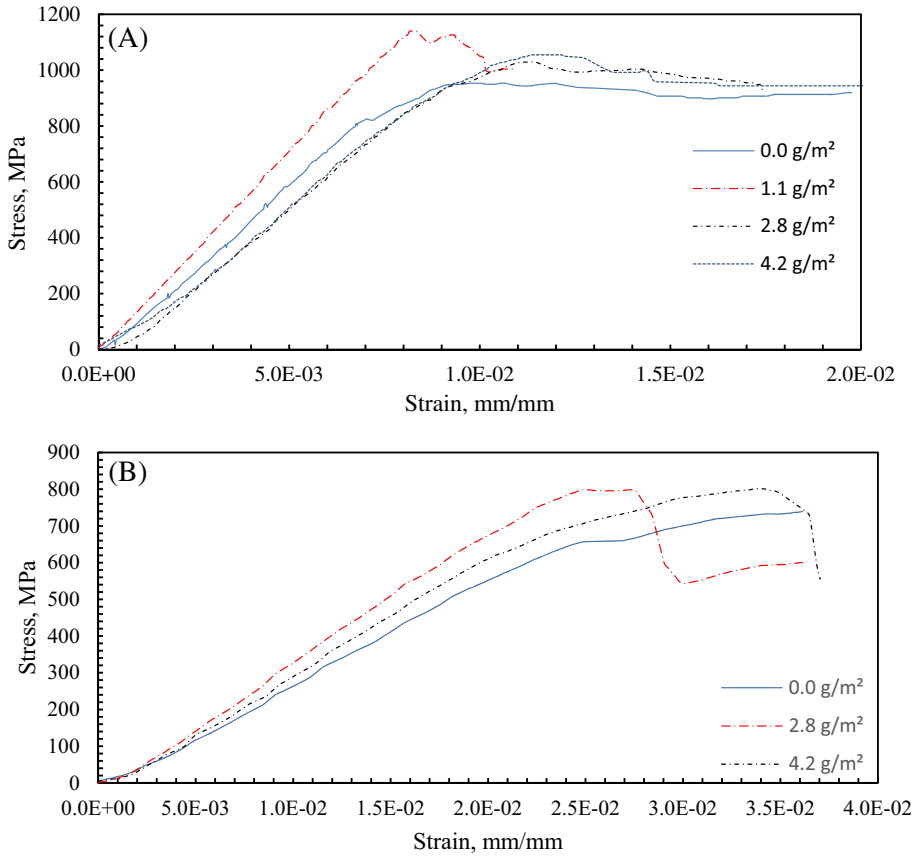

FIGURE 16 (A) Representative stress–strain curves for flexural beam testing. (B) Representative stress–strain curves for ILSS testing

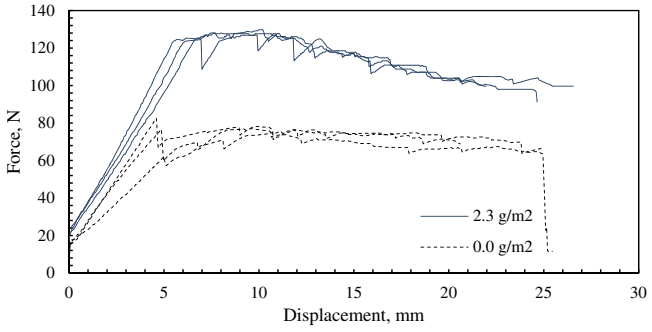

FIGURE 17 Load displacement curves for neat and 2.3 g/m^2 pGNP treated composites

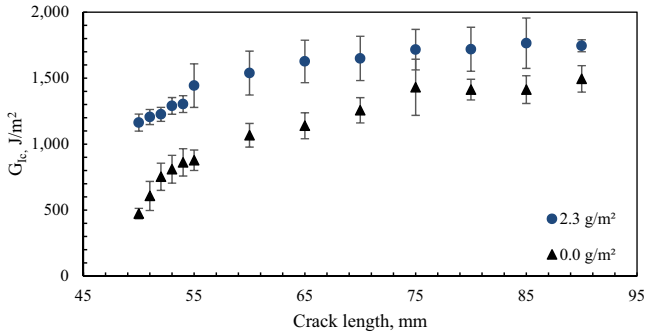

FIGURE 18 G_{Ic} values for CF/epoxy beams without treatment and with 2.3 g/m^2 pGNP interlaminar spray

surfaces in these studies has shown that nanoparticle pullout provides more reinforcement during opening mode fracture as opposed to sliding mode fracture where the particles provide less reinforcement.[47] Existing work has shown the improtance of alignment of nanoparticles on their properites in composite systems.[17]Given the strong performace of pGNP in mode I fracture, it is possible the spray deposition provides a particle alignment which is better suited for mode I fracture reinforcment than mode II. An alternate, or supporting explanation role of crack deflection as a mechanism for increasing fracture toughness as discussed above for mode I fracture. Crack deflection occures during the stable crack growth as a result of displacement-controlled mode of testing. Therefore, the unstable crack propagation during the Mode II test, does not support the increase in energy dissipation during ENF testing.

4 | CONCLUSIONS

Renewable pGNP offer an effective, plant-based alternative to other carbon nanoparticles, with a greater potential supply and reduced environmental impact. Using a mixed water/alcohol solvent, along with CMC and SDS as dispersion and viscosity modifiers, the dispersibility of

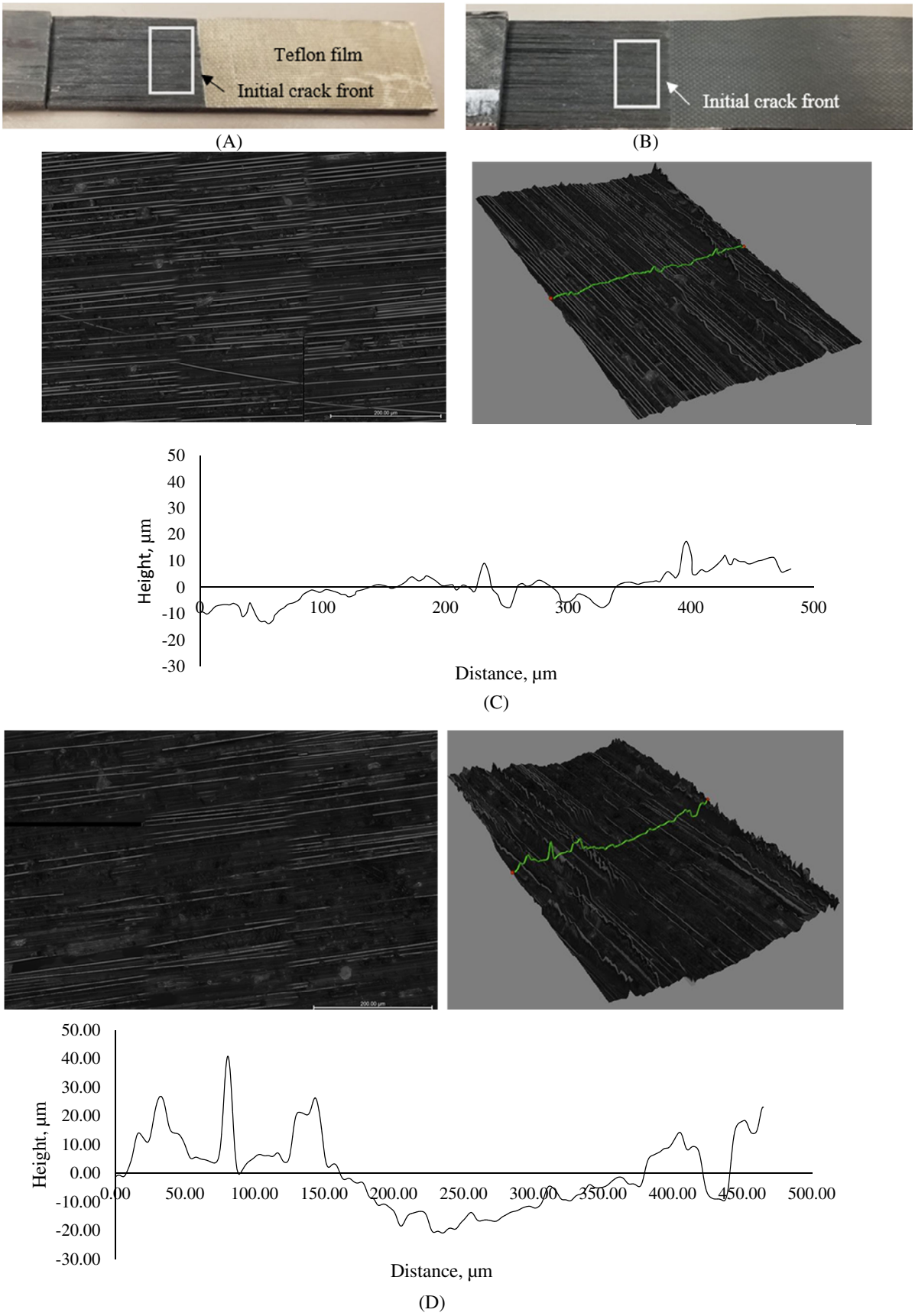

FIGURE 19 The scanned area of the micrographs for (A) untreated beam and (B) pGNP treated beam; (C) an untreaded beam and (D) pGNP treated beam

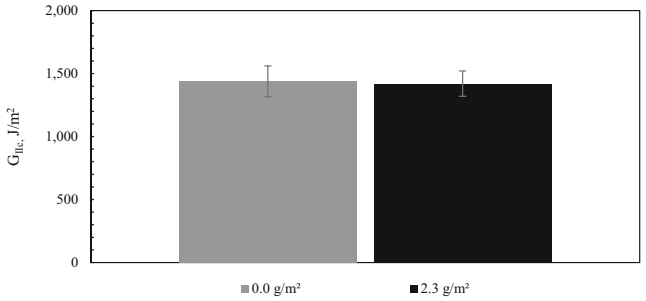

FIGURE 20 G_{IIc} values for CF/epoxy beams without treatment and with 2.3 g/m^2 pGNP interlaminar spray

pGNP were increased tenfold while providing a high surface energy and a desirable viscosity profile. The mix of water and alcohol as a solvent provides substantial increases to the surface energy and volatility of the suspension on uncured prepreg over water alone, which is desired to give fast, even drying and pGNP distribution on the prepreg surface. The water/alcohol mixture also gives substantial increase to the dispersibility of pGNP over an alcohol solvent. The addition of the surfactant SDS reduced the surface tension of the solvent at the pGNP/liquid interface and improves particle dispersibility by 1300%. CMC increases the low shear viscosity of the suspension, which is desirable for both the behavior of the sprayed pGNP layer as well as the dispersibility of the nanoparticles. CMC addition provided an 2900% increase in viscosity at 1 s^{-1} shear rate and a 1160% increase in suspended solids.

pGNP interlaminar addition by spray deposition increased the thermal and electrical conductivity of CF/epoxy samples at loadings as low as 1.1 g/m^2. The directional dependence on electrical conductivity offers potential to construct parts which are conductive in one direction more so than in others. Thermal conductivity exhibited a similar dependence on the fiber direction, which likewise suggests a possibility of creating directional conductivity, however, the evolution of voids at higher pGNP loading interfered with conductivity. Changes in the cure kinetics, shown by DSC and cure temperature testing, indicate that there is an interaction between the pGNP particles and the curing resin, which allows for stronger covalent bonds to form between epoxy and pGNP. With increase in pGNP loading, the peak curing temperature increased, as a result of lower through thickness conductivity and higher void content. The interaction between pGNP and resin curing warrants further study, as it may play a role in improved pGNP/epoxy material properties. XPS and SEM show that pGNP is distinct from exfoliated mineral GNP in morphology and functionality. The presence of carboxyl and epoxy functional groups contribute to improved dispersibility in suspension and reenforcing of resin. Epoxide and carboxyl functional groups on the pGNP surface are likely involved. Improvements to surface functional group utilization and curing dynamics present opportunities for improvements to strength and conductivity.

At lower loadings, from 1.1 to 2.8 g/m^2, every mechanical property showed significant improvement. The increases to ILSS (17%) represent an improvement to the load transfer between plies due to reinforcement of the interlaminar region which relates to the improvements in flexural strength (17%). Increases in flexural modulus (15%) at 1.1 g/m^2 represent an interlaminar region which is both stiffer and stronger than the untreated composite with pGNP addition.

Most significantly, the 146% increase to mode I fracture is a substantial improvement in one of the most common failure modes for composite materials and in increase over the results found in GNP studies of 101.5%.[27] This is consistent with flexural and short beam results which show that interlaminar pGNP addition provides substantial increases to the strength of the interlaminar region which results in crack front deflection and elongation. The deflection of the crack front increases the energy required to extend the crack in the stable, displacement-controlled mode I fracture. Mode II fracture was unaffected by pGNP addition, which corresponds with the model of crack front deflection since mode II fracture gives unstable crack propagation during the test, it does not support the increase in energy dissipation.

In every measured property, there was marginal utility of increased pGNP loading at higher levels, indicating optimal loading occurs at lower loadings. Future work will focus on loadings below 1.0 g/m^2 to optimize potential conductive and mechanical benefits.

ACKNOWLEDGMENTS

Dali Quan at University of Kentucky, Electron Microscopy Center for providing SEM, TEM and XPS data. Authors also acknowledge support from The Commonwealth Center for Innovation in Autonomous Systems.

ORCID

Daniel W. Mulqueen https://orcid.org/0000-0002-4314-2688
Siavash Sattar https://orcid.org/0000-0001-5175-8696
Oleksandr G. Kravchenko https://orcid.org/0000-0002-8573-7540

REFERENCES

[1] R. Singh, G. S. Sandhu, R. Penna, I. Farina, *Materials* **2017**, *10*, 881.
[2] L. M. Sherman, A Bright Future for Thermally Conductive Plastics, n.d. https://www.ptonline.com/articles/a-bright-future-for-thermally-conductive-plastics (accessed November 8, 2021).

[3] J. Liu, Y. Li, D. Xiang, C. Zhao, B. Wang, H. Li, *Appl. Compos. Mater.* **2021**, *28*, 17.
[4] Plastech, Graphene nanotubes in plastics are the basis for cars of the future, n.d. https://www.plastech.biz/en/news/Graphene-nanotubes-in-plastics-are-the-basis-for-cars-of-the-15628 (accessed November 8, 2021).
[5] R. Clark, *Real World Graphene: Industrial Applications for the 21st Century*, Material was presented at Graphite Spully Chain, Newport Beach, CA, USA **2017**.
[6] M. Campell, *EMI Shielding Solutions for Automotive FRP Composite Applications*, SPE Automotive ACCE Conference, Novi, MI, USA **2021**.
[7] A. K. Geim, K. S. Novoselov, *The Rise of Graphene*, Vol. 14 n.d. University of Manchester, Manchester, UK.
[8] A. Yu, P. Ramesh, M. E. Itkis, E. Bekyarova, R. C. Haddon, *J. Phys. Chem. C* **2007**, *111*, 7565.
[9] C.-C. Teng, L. C.-H. Ma C-CM, S.-Y. Yang, S.-H. Lee, M.-C. Hsiao, et al., *Carbon* **2011**, *49*, 5107.
[10] Y. Seki, E. Kizilkan, A. İşbilir, M. Sarikanat, L. Altay, *Polym. Compos.* **2021**, *42*, 4630.
[11] I. Jafari, M. Shakiba, F. Khosravi, S. Ramakrishna, E. Abasi, Y. S. Teo, M. Kalaee, M. Abdouss, A. Ramazani S. A, O. Moradi, E. Rezvani Ghomi, *Molecules* **2021**, *26*, 1597.
[12] P. S. Garcia, Y. D. C. Oliveira, F. C. F. Valim, R. Kotsilkova, E. Ivanov, R. K. Donato, G. J. M. Fechine, R. J. E. Andrade, *Polym. Compos.* **2021**, *42*, 6213.
[13] H. Liu, M. Dong, W. Huang, J. Gao, K. Dai, J. Guo, G. Zheng, C. Liu, C. Shen, Z. Guo, *J. Mater. Chem. C* **2017**, *5*, 73.
[14] N. D. Luong, U. Hippi, J. T. Korhonen, A. J. Soininen, J. Ruokolainen, L.-S. Johansson, J. D. Nam, L. H. Sinh, J. Seppälä, *Polymer* **2011**, *52*, 5237.
[15] E. C. Senis, I. O. Golosnoy, J. M. Dulieu-Barton, O. T. Thomsen, *J. Mater. Sci.* **2019**, *54*, 8955.
[16] K. A. Imran, K. N. Shivakumar, *J. Compos. Mater.* **2019**, *53*, 93.
[17] E. C. Senis, I. O. Golosnoy, T. Andritsch, J. M. Dulieu-Barton, O. T. Thomsen, *Polym. Compos.* **2020**, *41*, 3510.
[18] G. Gong, *Literature Study of Graphene Modified Polymeric Composites* n.d., p. 57. Sio Grafen, Pieta, Sweden **2018**.
[19] Y. T. Park, Y. Qian, C. Chan, T. Suh, M. G. Nejhad, C. W. Macosko, A. Stein, *Adv. Funct. Mater.* **2015**, *25*, 575.
[20] P. R. Thakre, D. C. Lagoudas, J. C. Riddick, T. S. Gates, S.-J. V. Frankland, J. G. Ratcliffe, Jiang Zhu, E. V. Barrera, *J. Compos. Mater.* **2011**, *45*, 1091.
[21] S. C. Joshi, V. Dikshit, *J. Compos. Mater.* **2012**, *46*, 665.
[22] O. G. Kravchenko, D. Pedrazzoli, D. Kovtun, X. Qian, I. Manas-Zloczower, *J. Phys. Chem. Solids* **2018**, *112*, 163.
[23] O. G. Kravchenko, D. Pedrazzoli, V. S. Bonab, I. Manas-Zloczower, *Mater. Des.* **2018**, *160*, 1217.
[24] O. G. Kravchenko, V. Solouki Bonab, I. Manas-Zloczower, *Polym. Eng. Sci.* **2019**, *59*, 2247.
[25] K. Almuhammadi, M. Alfano, Y. Yang, G. Lubineau, *Mater. Des.* **2014**, *53*, 921.
[26] H. Zhang, Y. Liu, M. Kuwata, E. Bilotti, T. Peijs, *Compos. Part Appl. Sci. Manuf.* **2015**, *70*, 102.
[27] B. Liu, S. Cao, N. Gao, L. Cheng, Y. Liu, Y. Zhang, D. Feng, *Compos. Sci. Technol.* **2019**, *183*, 107829.
[28] D. W. Johnson, B. P. Dobson, K. S. Coleman, *Curr. Opin. Colloid Interface Sci.* **2015**, *20*, 367.
[29] N. H. Md Said, W. Liu, C. Khe, C. Lai, N. N. Zulkepli, A. Aziz, *Polym. Compos.* **2021**, *42*, 1075.
[30] D. Mulqueen, O. G. Kravchenko, Improving Thermal and Electrical Conductivity Of Thermosetting Composites With Plant-Based Graphene, *SPE Automotive ACCE Conference*, **2021**, Novi, MI, USA.
[31] V. Vignesh, N. Nagaprasad, N. B. Karthik Babu, P. Manimaran, B. Stalin, K. Ramaswamy, *Polym. Compos.* **2022**, *1*, pc.26925. https://doi.org/10.1002/pc.26925
[32] A. Pizza, R. Metz, M. Hassanzadeh, J.-L. Bantignies, *Int. J. Life Cycle Assess.* **2014**, *19*, 1226.
[33] M. Cossutta, J. McKechnie, S. J. Pickering, *Comparative LCA of Different Graphene Production Routes*, Vol. 18 n.d., University of Nottingham, Nottingham, UK **2017**.
[34] L. Serrano-Luján, S. Víctor-Román, C. Toledo, O. Sanahuja-Parejo, A. E. Mansour, J. Abad, A. Amassian, A. M. Benito, W. K. Maser, A. Urbina, *SN Appl. Sci.* **2019**, *1*, 179.
[35] R. Arvidsson, *Adv. Mater. Lett.* **2017**, *8*, 187.
[36] R. Bergman, M. Puettmann, A. Taylor, K. E. Skog, *For. Prod. J.* **2014**, *64*, 220.
[37] E. George, J. Joy, S. Anas, *Polym. Compos.* **2021**, *42*, 4961.
[38] N. Crawford, F. Meyer, *Investigating the Shear Flow and Thixotropic Behavior of Paints and Coatings* n.d., p. 4. Thermo Fisher Scientific, Karlsruhe, Germany, **2019**.
[39] R. R. Eley, *J. Coat. Technol. Res.* **2019**, *16*, 263.
[40] Polarity Index, n.d. https://macro.lsu.edu/howto/solvents/polarity%20index.htm (accessed August 9, 2022).
[41] M. Hassan, K. R. Reddy, E. Haque, A. I. Minett, V. G. Gomes, *J. Colloid Interface Sci.* **2013**, *410*, 43.
[42] N. T. Kamar, M. M. Hossain, A. Khomenko, M. Haq, L. T. Drzal, A. Loos, *Compos. Part Appl. Sci. Manuf.* **2015**, *70*, 82.
[43] O. G. Kravchenko, S. G. Kravchenko, C.-T. Sun, *Compos. Struct.* **2017**, *160*, 538.
[44] M. S. Chaudhry, A. Czekanski, Z. H. Zhu, *Int. J. Mech. Sci.* **2017**, *131–132*, 480.
[45] K. Mishra, K. P. Bastola, R. P. Singh, R. Vaidyanathan, *Polym. Eng. Sci.* **2019**, *59*, 1199.
[46] C. S. Nagi, S. L. Ogin, I. Mohagheghian, C. Crean, A. D. Foreman, *Mater. Des.* **2020**, *193*, 108831.
[47] J. A. Rodríguez-González, C. Rubio-González, *Adv. Compos. Mater.* **2018**, *28*, 1. https://doi.org/10.1080/09243046.2018.1458510

How to cite this article: D. W. Mulqueen, S. Sattar, T. Le, O. G. Kravchenko, *Polym. Compos.* **2022**, *43*(12), 8696. https://doi.org/10.1002/pc.27051